

Phononic bath engineering of a superconducting qubit

J. M. Kitzman^{1,*}, J. R. Lane¹, C. Undershute¹, P. M. Harrington²,
N. R. Beysengulov¹, C. A. Mikolas¹, K. W. Murch³, J. Pollanen^{1†}

¹*Department of Physics and Astronomy,*

Michigan State University, East Lansing, MI 48824, USA

²*Research Laboratory of Electronics,*

Massachusetts Institute of Technology, Cambridge, MA 02139, USA

³*Department of Physics, Washington University in St. Louis, St. Louis, MO 63130, USA*

Phonons, the ubiquitous quanta of vibrational energy, play a vital role in the performance of many quantum technologies. Coupling to well-defined phonon modes allows for highly-connected multi-qubit gates in ion trap architectures [1–3] as well as the generation of entangled states in systems of superconducting qubits [4, 5]. Even when the phonons take the form of a large dissipative bath, an irreversible flow of heat allows for state initialization critical to the function of laser systems [6] and the operation of optically active spin qubits [7, 8]. Conversely, unintended coupling to phonons has been shown to degrade qubit performance by generating decohering quasiparticles and leading to correlated errors in superconducting qubit systems [9–12]. Regardless of whether a phononic bath plays an enabling or deleterious role, it is typically intrinsic to the system and does not admit specific control over its spectral properties, nor the possibility of engineering aspects of its dissipation to be used as a resource. Here we show that by precisely designing and controlling the coupling of a superconducting qubit to phononic degrees of freedom allows a new type of quantum control over superconducting circuits. By shaping the loss spectrum of the qubit via its coupling to a bath of lossy piezoelectric surface acoustic wave phonons, we are able to prepare and stabilize arbitrary qubit states. Additionally, we find that the presence of the energy-dependent loss imparted onto the qubit by the phonons is well-described by a master equation treatment of the composite system, with excellent agreement in both the qubit dynamics as well as its steady state. Our results demonstrate the ability of engineered phononic dissipation to achieve highly efficient qubit control.

Hybrid quantum systems based on the coherent coupling of two or more distinct, but interacting, systems enable the development of advanced quantum technologies [13], and investigation into the fundamental properties of complex interacting quantum degrees of freedom. Hybrid systems based on superconducting qubits, utilizing the experimental tool-kit of circuit quantum electrodynamics (cQED) [14], are a versatile platform for creating and controlling heterogeneous quantum systems and investigating their coherent dynamics [15]. Of particular interest is the ability to leverage the intrinsically strong nonlinearity provided by the qubit to manipulate collective mechanical and acoustic degrees of freedom and explore new regimes of circuit quantum optics using GHz-frequency phonons. By engineering strong in-

interactions between superconducting qubits and mechanical resonators it is possible to study the quantum limits of high-frequency sound in a wide variety of systems composed of qubits coupled to bulk phonons [16, 17], Rayleigh-like surface waves [18–24], as well as flexural modes in suspended structures [25–27]. Impressive experimental results have been demonstrated using integrated quantum acoustic systems, including single phonon splitting of the qubit spectrum [28–30], Wigner function negativity of an acoustic resonator [16, 21, 30, 31], electromagnetically induced acoustic transparency [24], and phonon mediated state transfer [4, 5].

Hybrid quantum acoustics systems that integrate superconducting qubits with phononic degrees of freedom typically operate in a domain where the interaction strength between the two far exceeds the loss rate of either system. In this strong coupling regime, the emphasis is on the coherent dynamics of the coupled systems rather than on the dissipation presented to the qubit via the phononic bath. However, the ability to create quantum acoustic systems in which the qubit may be variably coupled to multiple mechanical degrees of freedom with vastly differing strengths and loss rates opens the door for dissipative state preparation and stabilization via customized phononic loss channels. Piezoelectric surface acoustic wave (SAW) devices, which can be engineered into compact devices with sharp spectral responses at telecom frequencies [19–21], are a promising avenue for engineering highly frequency dependent phononic dissipation channels for quantum bath engineering protocols, in which the level of surface wave dissipation and qubit coupling can be precisely designed and controlled (see Fig. 1(a)).

We implement a quantum acoustic bath engineering protocol using a hybrid quantum system consisting of a flux-tunable transmon qubit coupled to a SAW Fabry Péro cavity fabricated on the surface of single crystal lithium niobate (see Fig. 1 and Methods). The complex admittance that describes the electro-mechanical properties of the SAW device, and tailors the coupling to the phonon bath, are calculated using the coupling-of-modes method [32, 33] (see Supplemental Information). The qubit and SAW resonator are fabricated on separate substrates and their purely capacitive coupling is mediated in a flip-chip geometry via antenna pads attached to each device in the form of a pair of parallel plate capacitors (see Fig. 1). For control and readout, the composite flip-chip device is free-space coupled to the fundamental mode of a three-dimensional (3D) electromagnetic cavity with a frequency of $\omega_c/(2\pi) = 4.788$ GHz.

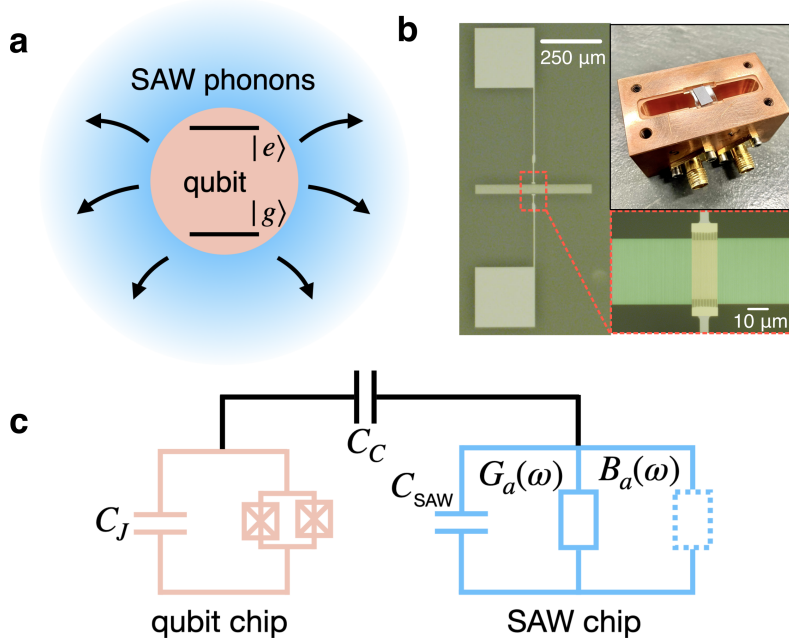


FIG. 1. (a) Schematic representing a qubit coupled to a bath of SAW phonons. The qubit (salmon) non-unitarily radiates excitations into a bath of SAW phonons (blue), where the emission rate is mediated by the electrical conductance of the SAW structure. (b) Image of the SAW device (left) and the flip-chip qubit-SAW hybrid device mounted in a 3D microwave cavity (top right), which is used for control and readout. False color optical micrograph of the acoustic resonator (bottom right), consisting of an IDT (yellow), as well as acoustic Bragg mirrors (green). (c) Equivalent circuit model of the composite qubit-SAW system. Here C_J is the total capacitance shunting the Josephson junctions, C_C is the capacitance responsible for coupling the qubit and SAW resonator, which is primarily dictated by the parallel-plate capacitance between the two substrates, and C_{SAW} is the geometric capacitance of the SAW resonator. The complex admittance that represents the electro-mechanic response of the SAW resonator is divided into a conductance $G_a(\omega)$, as well as a susceptance $B_a(\omega)$ (see Supplemental Information).

As shown in Fig. 2(a), we design the SAW resonator spectral response in order to access both its coherent coupling to the transmon as well as the dissipative qubit-phonon dynamics. The SAW resonator is engineered to confine a single acoustic mode, which appears as a sharp peak in the conductance of the resonator near 4.46 GHz (see Fig. 2(a) and Supplemental Information). On either side of this main SAW resonance, phononic energy loss is governed by a continuum of dissipative SAW states that manifest as frequency ripples in the effective

conductance of the acoustic resonator and correspond to the leakage of surface-phonons out of the SAW resonator through the acoustic Bragg mirrors (see Fig. 1(b)). Measurements shown in Fig. 2(b) reveal how the features of the SAW resonator response are imparted onto the spectroscopic properties of the hybrid system and enable access to multiple regimes of circuit quantum acoustodynamics (cQAD) [20]. The qubit and the confined SAW mode interact with a coupling rate $g_m/(2\pi) = 12 \pm 0.6$ MHz, larger than the loss rate of either system, which is a hallmark of the quantum acoustic strong coupling regime. Importantly, the spectroscopy also reveals signatures of controlled surface phonon loss arising from the interaction of the qubit with the continuum of SAW modes on either side of the confined SAW mode. This interaction manifests as a series of dark states in the qubit spectrum, which appear as horizontal fringes in Fig. 2(b), and corresponds to the acoustic analog of the bad-cavity limit of cQED [14]. In this dissipative regime the dynamics of the hybrid system is dominated by the loss of phonons from the resonator that have a frequency outside of the acoustic mirror stop band (see Supplemental Information).

To utilize the frequency-dependent acoustic loss for quantum state stabilization, we consider the effect of phononic decay on qubit decoherence. In the case of a strong coherent drive of amplitude Ω near resonant with the qubit, the emission spectrum the system consists of a peak at the drive frequency ω_d and two additional sidebands at $\omega_d \pm \Omega_R$, where $\Omega_R = \sqrt{\Omega^2 + \Delta^2}$ is the generalized Rabi frequency and $\Delta = \omega_d - \omega_q$ is the detuning between the drive and the qubit [34–36] (see Fig. 3 (a)). In the presence of a frequency-dependent emission spectrum, one sideband can be suppressed, leading to preferential emission from the other sideband and non-zero qubit coherence in the undriven basis for times long compared to the intrinsic lifetime of the qubit [37].

For this type of bath engineering protocol to work in our device, the SAW admittance must modify the decoherence rate of the qubit over frequencies comparable to experimentally accessible values of Ω_R . To verify this, we measured the qubit decay rate $\Gamma_q = 1/T_1$ across a broad range of frequencies far-detuned from the main acoustic resonance (see Fig. 3(b)) where phonon leakage through the acoustic mirrors is maximized. At these frequencies, the conductance of the SAW resonator is well approximated by that of the acoustic transducer, as the reflectivity of the acoustic Bragg mirrors is small, and the total loss of the qubit can

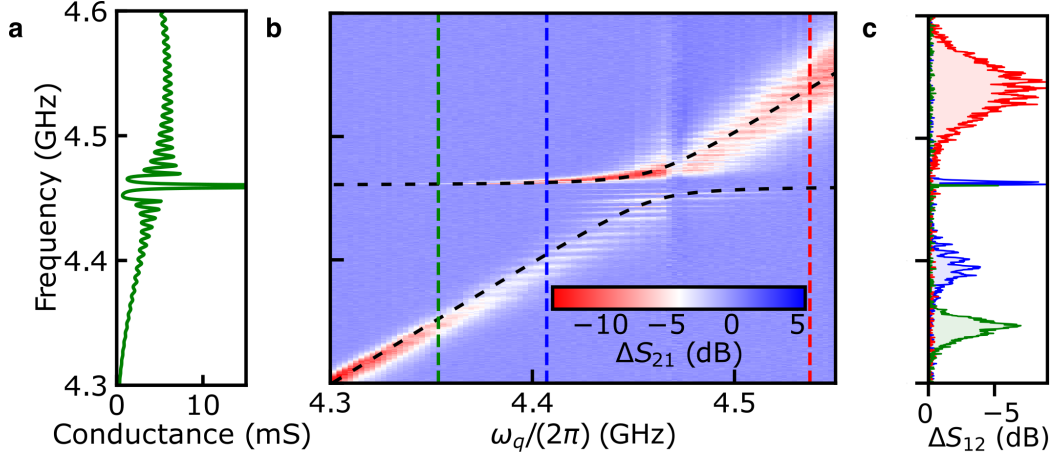


FIG. 2. (a) Simulation of the SAW resonator conductance $G_a(\omega)$ based on the coupling-of-modes modeling (see Supplemental Information). The resonator is designed to host a single confined SAW mode, which corresponds to the narrow peak in the device conductance at 4.46 GHz, and the effective electrical conductance of the device mediates the coupling between the qubit and a given SAW mode. (b) Two-tone spectroscopy of the SAW-qubit hybrid system revealing an avoided crossing between the qubit and main SAW mode. Black dashed line: fit to the data, indicating an acoustic coupling of $g_m/(2\pi) = 12 \pm 0.6$ MHz. (c) Spectroscopy line-cuts from (b) at the positions of the vertical dashed lines. The oscillations in frequency in each scan highlight the phononic loss channel imparted on the qubit, which arise from the modulation of the conductance of the SAW resonator and are associated with the leakage of SAW excitations through the acoustic Bragg mirrors.

be approximated as:

$$\Gamma_q(\omega_q) = \frac{\omega_q}{Q_i} + \Gamma_0 \operatorname{sinc}^2\left(\pi N_p \frac{\omega_q - \omega_s}{\omega_s}\right), \quad (1)$$

where $Q_i = 1.05 \times 10^4$ is the qubit internal quality factor, $\Gamma_0 = 0.252 \text{ ns}^{-1}$ is the maximum conversion rate of the qubit excitation into SAW phonons, $N_p = 16$ is the number of finger pairs in the IDT structure of the SAW resonator, and $\omega_s/(2\pi) = 4.504$ GHz is the central SAW frequency, which is within 1% of the value predicted from the device fabrication parameters (see Supplemental Information). At $\omega_q/(2\pi) = 4.001$ GHz, where the gradient of qubit loss into SAW phonons is large, the qubit decay rate varies by a factor of 3.7 over a span of 80 MHz ($\approx 2\Omega_R$) and allows us to use SAW phonon modes for efficient state preparation.

The dynamics of the reduced qubit density matrix in the combined presence of the drive

and frequency-dependent SAW loss are described by the Lindblad master equation [37–39]:

$$\begin{aligned} \dot{\rho} = & i[\rho, H] + \gamma_0 \cos^2(\theta) \sin^2(\theta) \mathcal{D}[\tilde{\sigma}_z] \rho + \gamma_- \sin^4(\theta) \mathcal{D}[\tilde{\sigma}_+] \rho \\ & + \gamma_+ \cos^4(\theta) \mathcal{D}[\tilde{\sigma}_-] \rho + \gamma_1 \mathcal{D}[\sigma_-] \rho + \gamma_\phi \mathcal{D}[\sigma_z] \rho, \end{aligned} \quad (2)$$

where $\mathcal{D}[A]\rho = (2A\rho A^\dagger - A^\dagger A\rho - \rho A^\dagger A)/2$. The angle θ is defined by $\tan 2\theta = -\Omega/\Delta$ and represents the rotation of the qubit eigenbasis under the drive (see Fig. 3(a) and Supplemental Information). The operators $\tilde{\sigma}_\pm$ and $\tilde{\sigma}_z$ along with the corresponding rates γ_\pm and γ_0 represent transitions between eigenstates and dephasing in the rotated frame. Dissipation in the lab frame is represented by the operators σ_- and σ_z along with the rates γ_1 and γ_ϕ , for qubit depolarization and dephasing. The transition rates γ_\pm represent competing decay of the qubit into SAW phonons in the rotated basis, and by tailoring the frequency-dependent phonon bath these rates vary significantly over the frequency scale $2\Omega_R$ as seen in Fig. 3(b). In the limit $\gamma_\pm \gg \gamma_\mp$, the spectral weight of one sideband of the qubit emission spectrum is suppressed, leading to stabilization of a rotating-frame eigenstate.

To demonstrate the phononic bath engineering protocol, we flux bias the qubit to $\omega_q/(2\pi) = 4.001$ GHz, where the gradient of the qubit loss varies strongly as a function of frequency (see Fig. 3(b)). By tailoring the drive parameters the qubit emits radiation at frequencies corresponding to Mollow triplet sidebands [34] at rates governed by the SAW-phonon induced loss. By driving the qubit at a detuning $\Delta/(2\pi) = -10$ MHz with strength $\Omega/(2\pi) = 8.57$ MHz we are able to prepare an arbitrary qubit state in the XZ -plane of the Bloch sphere, which we verify using tomographic reconstruction of the qubit state as a function of driving time t_{drive} . As shown in Fig. 3(c), in the limit $t_{\text{drive}} \rightarrow \infty$, the qubit density matrix approaches a fixed point determined by the drive parameters and asymmetric phononic loss. We further quantify this dissipation-enabled stabilization protocol by calculating the state purity of the qubit, $\mathcal{P} = \text{Tr}(\rho^2)$, as a function of time as shown in Fig. 3(d). We see that, in the limit $t_{\text{drive}} \rightarrow \infty$, the state purity reaches $\mathcal{P} = 0.85$, well above the value $\mathcal{P} = 0.5$ of a maximally mixed state. By including the global dephasing rate $\gamma_\phi = 0.75 \mu\text{s}^{-1}$ and global depolarization rate of $\gamma_1 = 2.565 \mu\text{s}^{-1}$ in the numerical solutions to Eq. 2, we find quantitative agreement to the tomography data shown in Fig. 3(c,d), indicating that this particular superposition state is cooled to an effective temperature $T_{\text{eff}} \simeq 900 \mu\text{K}$ [40].

In the combined presence of drive and phonon loss through the mirrors, the steady-state of the qubit should exhibit coherence on timescales long to the intrinsic qubit lifetime in the

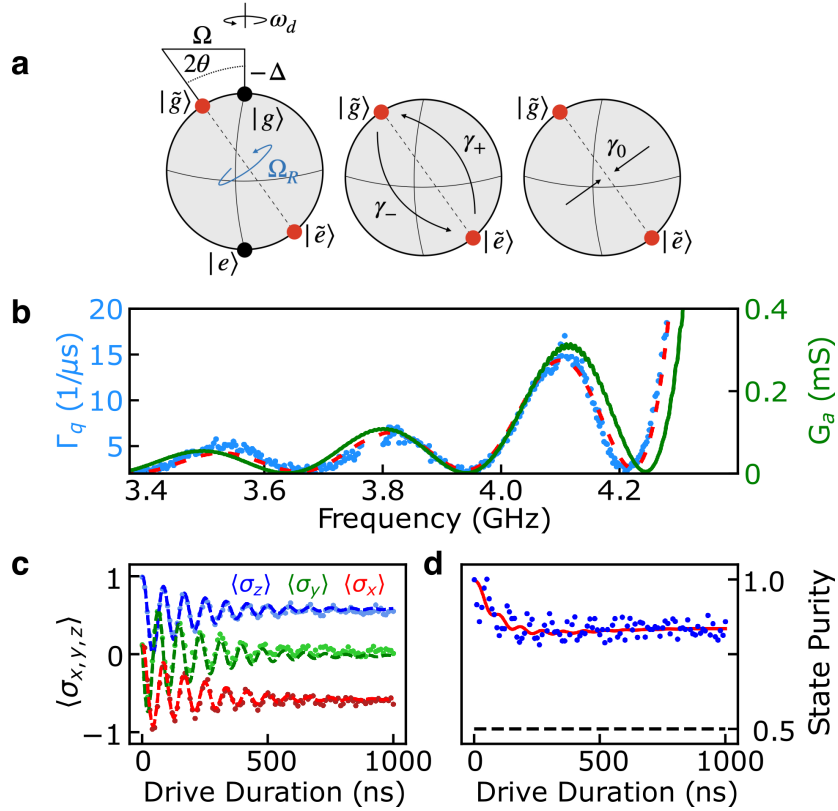


FIG. 3. (a) Left: schematic representing the rotation of the qubit eigenbasis in the presence of a detuned drive applied to the qubit. Center: representation of competing decay rates in the dressed qubit basis. By tailoring the coupling of the qubit to the frequency-dependent phonon bath, we are able to control the relative size of γ_{\pm} as a function of qubit frequency. Right: representation of pure dephasing in the dressed basis. (b) Measurement of qubit loss $\Gamma_q = 1/T_1$ versus frequency (blue). The red curve is a fit to Eq. 1 showing that the variation in the qubit loss is dictated by conversion into SAW phonons. The green curve is a result of coupling-of-modes model for the electrical conductance of the SAW resonator with no fit parameters (see Supplemental Information). (c) Tomographic reconstruction of qubit state evolution at a resonant Rabi frequency of $\Omega/(2\pi) = 8.57$ MHz and drive detuning $\Delta/(2\pi) = -10$ MHz. Dots represent the experimental data while the dashed lines are solutions to Eq. 2 with the same drive parameters. (d) Measurement of the state purity as a function of time. In the combined presence of phonon loss and drive the purity reaches a value of 0.85 at $t = 1 \mu\text{s}$, in contrast to a maximally mixed state represented by the dashed line at $\mathcal{P} = 0.5$.

lab frame. To investigate this steady-state behavior, we apply a coherent drive to the qubit for a preparation time $t_{\text{prep}} = 3 \mu\text{s}$, which is approximately one order of magnitude longer than the measured depolarization time of the qubit in the absence of drive (see Fig. 4(a)). By choosing the parameters of the drive, we control both the rotation of the qubit eigenstates as well as the splitting of the Mollow triplet sidebands, which modifies their coupling to the lossy phononic bath. We tomographically reconstruct the steady-state expectation value $\langle \sigma_x \rangle = \text{Tr}(\rho \sigma_x)$ in the bare qubit eigenbasis as a function of drive parameters and compare with solutions to Eq. 2 as shown in Fig. 4(b,c). As we modify the coupling between the qubit and SAW-phonon bath, we observe excellent agreement between the measured and predicted purity of the qubit state, and reveal a region of zero coherence where the competing loss rates γ_{\pm} in Eq. 2 cancel each other and the qubit reaches a maximally mixed state.

In conclusion, we have demonstrated coupling of a superconducting qubit to an engineered

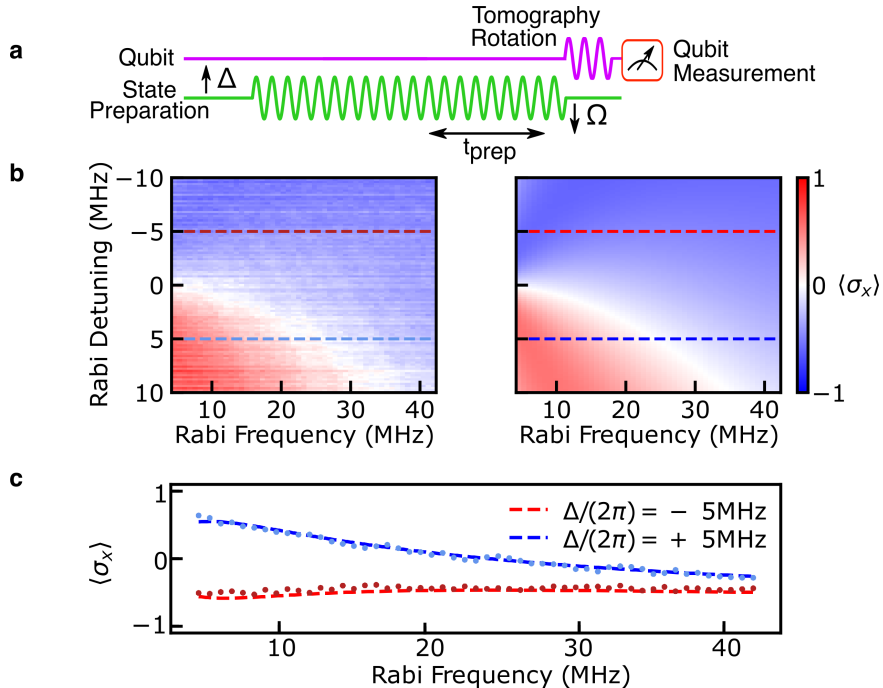


FIG. 4. (a) Pulse sequence for investigating the steady-state coherence of the driven-dissipative quantum acoustics system. (b) By varying both the strength (resonant Rabi frequency) and the detuning of the state preparation pulse relative to the qubit frequency we are able to demonstrate state stabilization that has both positive and negative values of $\langle \sigma_x \rangle$, in good agreement with solutions to Eq. 2. (c) Representative horizontal linecuts from (b) along with the corresponding predictions based of the solution to the Lindblad master equation (Eq. 2)

bath of lossy surface acoustic wave phonons where phononic dissipation is the dominant process governing the time evolution of qubit states. Controlling phononic loss in this way allows for high-purity arbitrary qubit state preparation and stabilization. Modest improvements to the transducer design and qubit quality factor offer an avenue to prepare states with purity exceeding 99%. These results also open the door to investigating the non-unitary evolution of quantum states and effective non-Hermitian Hamiltonians hosting decoherence-induced exceptional points in open quantum acoustic systems via post-selection protocols [41].

* kitzmanj@msu.edu

† pollanen@msu.edu

- [1] J. I. Cirac and P. Zoller, Quantum computations with cold trapped ions, *Phys. Rev. Lett.* **74**, 4091 (1995).
- [2] J. I. Cirac and P. Zoller, A scalable quantum computer with ions in an array of microtraps, *Nature* **404**, 579 (2000).
- [3] S.-L. Zhu, C. Monroe, and L.-M. Duan, Trapped ion quantum computation with transverse phonon modes, *Phys. Rev. Lett.* **97**, 050505 (2006).
- [4] A. Bienfait, K. J. Satzinger, Y. P. Zhong, H.-S. Chang, M.-H. Chou, C. R. Conner, É. Dumur, J. Grebel, G. A. Peairs, R. G. Povey, and A. N. Cleland, Phonon-mediated quantum state transfer and remote qubit entanglement, *Science* **364**, 368 (2019), <https://science.sciencemag.org/content/364/6438/368.full.pdf>.
- [5] É. Dumur, K. J. Satzinger, G. A. Peairs, M.-H. Chou, A. Bienfait, H.-S. Chang, C. R. Conner, J. Grebel, R. G. Povey, Y. P. Zhong, and A. N. Cleland, Quantum communication with itinerant surface acoustic wave phonons, *npj Quantum Information* **7**, 173 (2021).
- [6] C. V. Shank, Physics of dye lasers, *Rev. Mod. Phys.* **47**, 649 (1975).
- [7] R. Hanson, O. Gywat, and D. D. Awschalom, Room-temperature manipulation and decoherence of a single spin in diamond, *Phys. Rev. B* **74**, 161203 (2006).
- [8] W. F. Koehl, B. B. Buckley, F. J. Heremans, G. Calusine, and D. D. Awschalom, Room temperature coherent control of defect spin qubits in silicon carbide, *Nature* **479**, 84 (2011).
- [9] U. Patel, I. V. Pechenezhskiy, B. L. T. Plourde, M. G. Vavilov, and R. McDermott, Phonon-mediated quasiparticle poisoning of superconducting microwave resonators, *Phys. Rev. B* **96**,

- 220501 (2017).
- [10] A. Bargerbos, L. J. Splitthoff, M. Pita-Vidal, J. J. Wesdorp, Y. Liu, P. Krogstrup, L. P. Kouwenhoven, C. K. Andersen, and L. Grünhaupt, Mitigation of quasiparticle loss in superconducting qubits by phonon scattering (2022).
 - [11] C. D. Wilen, S. Abdullah, N. A. Kurinsky, C. Stanford, L. Cardani, G. D’Imperio, C. Tomei, L. Faoro, L. B. Ioffe, C. H. Liu, A. Opremcak, B. G. Christensen, J. L. DuBois, and R. McDermott, Correlated charge noise and relaxation errors in superconducting qubits, *Nature* **594**, 369 (2021).
 - [12] M. McEwen, L. Faoro, K. Arya, A. Dunsworth, T. Huang, S. Kim, B. Burkett, A. Fowler, F. Arute, J. C. Bardin, A. Bengtsson, A. Bilmes, B. B. Buckley, N. Bushnell, Z. Chen, R. Collins, S. Demura, A. R. Derk, C. Erickson, M. Giustina, S. D. Harrington, S. Hong, E. Jeffrey, J. Kelly, P. V. Klimov, F. Kostritsa, P. Laptev, A. Locharla, X. Mi, K. C. Miao, S. Montazeri, J. Mutus, O. Naaman, M. Neeley, C. Neill, A. Opremcak, C. Quintana, N. Redd, P. Roushan, D. Sank, K. J. Satzinger, V. Shvarts, T. White, Z. J. Yao, P. Yeh, J. Yoo, Y. Chen, V. Smelyanskiy, J. M. Martinis, H. Neven, A. Megrant, L. Ioffe, and R. Barends, Resolving catastrophic error bursts from cosmic rays in large arrays of superconducting qubits, *Nature Physics* **18**, 107 (2022).
 - [13] G. Kurizki, P. Bertet, Y. Kubo, K. Mølmer, D. Petrosyan, P. Rabl, and J. Schmiedmayer, Quantum technologies with hybrid systems, *Proceedings of the National Academy of Sciences* **112**, 3866 (2015), <https://www.pnas.org/content/112/13/3866.full.pdf>.
 - [14] A. Blais, A. L. Grimsmo, S. M. Girvin, and A. Wallraff, Circuit quantum electrodynamics, *Rev. Mod. Phys.* **93**, 025005 (2021).
 - [15] A. A. Clerk, K. W. Lehnert, P. Bertet, J. R. Petta, and Y. Nakamura, Hybrid quantum systems with circuit quantum electrodynamics, *Nature Physics* **16**, 257 (2020).
 - [16] Y. Chu, P. Kharel, T. Yoon, L. Frunzio, P. T. Rakich, and R. J. Schoelkopf, Creation and control of multi-phonon fock states in a bulk acoustic-wave resonator, *Nature* **563**, 666 (2018).
 - [17] Y. Chu, P. Kharel, W. H. Renninger, L. D. Burkhardt, L. Frunzio, P. T. Rakich, and R. J. Schoelkopf, Quantum acoustics with superconducting qubits, *Science* **358**, 199 (2017), <https://www.science.org/doi/pdf/10.1126/science.aao1511>.
 - [18] M. V. Gustafsson, T. Aref, A. F. Kockum, M. K. Ekström, G. Johansson, and P. Delsing, Propagating phonons coupled to an artificial atom, *Science* **346**, 207 (2014),

<https://www.science.org/doi/pdf/10.1126/science.1257219>.

- [19] T. Aref, P. Delsing, M. K. Ekström, A. F. Kockum, M. V. Gustafsson, G. Johansson, P. J. Leek, E. Magnusson, and R. Manenti, Quantum acoustics with surface acoustic waves, in *Superconducting Devices in Quantum Optics*, edited by R. H. Hadfield and G. Johansson (Springer International Publishing, Cham, 2016) pp. 217–244.
- [20] R. Manenti, A. F. Kockum, A. Patterson, T. Behrle, J. Rahamim, G. Tancredi, F. Nori, and P. J. Leek, Circuit quantum acoustodynamics with surface acoustic waves, *Nature Communications* **8**, 975 (2017).
- [21] K. J. Satzinger, Y. P. Zhong, H.-S. Chang, G. A. Peairs, A. Bienfait, M.-H. Chou, A. Y. Cleland, C. R. Conner, É. Dumur, J. Grebel, I. Gutierrez, B. H. November, R. G. Povey, S. J. Whiteley, D. D. Awschalom, D. I. Schuster, and A. N. Cleland, Quantum control of surface acoustic-wave phonons, *Nature* **563**, 661 (2018).
- [22] B. A. Moores, L. R. Sletten, J. J. Viennot, and K. W. Lehnert, Cavity quantum acoustic device in the multimode strong coupling regime, *Phys. Rev. Lett.* **120**, 227701 (2018).
- [23] P. Delsing, A. N. Cleland, M. J. A. Schuetz, J. Knörzer, G. Giedke, J. I. Cirac, K. Srinivasan, M. Wu, K. C. Balram, C. Bäuerle, T. Meunier, C. J. B. Ford, P. V. Santos, E. Cerda-Méndez, H. Wang, H. J. Krenner, E. D. S. Nysten, M. Weiß, G. R. Nash, L. Thevenard, C. Gourdon, P. Rovillain, M. Marangolo, J.-Y. Duquesne, G. Fischerauer, W. Ruile, A. Reiner, B. Paschke, D. Denysenko, D. Volkmer, A. Wixforth, H. Bruus, M. Wiklund, J. Reboud, J. M. Cooper, Y. Fu, M. S. Bruggner, F. Rehfeldt, and C. Westerhausen, The 2019 surface acoustic waves roadmap, *Journal of Physics D: Applied Physics* **52**, 353001 (2019).
- [24] G. Andersson, M. K. Ekström, and P. Delsing, Electromagnetically induced acoustic transparency with a superconducting circuit, *Phys. Rev. Lett.* **124**, 240402 (2020).
- [25] M. D. LaHaye, J. Suh, P. M. Echternach, K. C. Schwab, and M. L. Roukes, Nanomechanical measurements of a superconducting qubit, *Nature* **459**, 960 (2009).
- [26] J.-M. Pirkkalainen, S. U. Cho, J. Li, G. S. Paraoanu, P. J. Hakonen, and M. A. Sillanpää, Hybrid circuit cavity quantum electrodynamics with a micromechanical resonator, *Nature* **494**, 211 (2013).
- [27] A. P. Reed, K. H. Mayer, J. D. Teufel, L. D. Burkhardt, W. Pfaff, M. Reagor, L. Sletten, X. Ma, R. J. Schoelkopf, E. Knill, and K. W. Lehnert, Faithful conversion of propagating quantum information to mechanical motion, *Nature Physics* **13**, 1163 (2017).

- [28] L. R. Sletten, B. A. Moores, J. J. Viennot, and K. W. Lehnert, Resolving phonon Fock states in a multimode cavity with a double-slit qubit, *Phys. Rev. X* **9**, 021056 (2019).
- [29] P. Arrangoiz-Arriola, E. A. Wollack, Z. Wang, M. Pechal, W. Jiang, T. P. McKenna, J. D. Witmer, R. Van Laer, and A. H. Safavi-Naeini, Resolving the energy levels of a nanomechanical oscillator, *Nature* **571**, 537 (2019).
- [30] U. von Lüpkke, Y. Yang, M. Bild, L. Michaud, M. Fadel, and Y. Chu, Parity measurement in the strong dispersive regime of circuit quantum acoustodynamics, *Nature Physics* 10.1038/s41567-022-01591-2 (2022).
- [31] E. A. Wollack, A. Y. Cleland, R. G. Gruenke, Z. Wang, P. Arrangoiz-Arriola, and A. H. Safavi-Naeini, Quantum state preparation and tomography of entangled mechanical resonators, *Nature* **604**, 463 (2022).
- [32] D. P. Morgan, *Surface Acoustic Wave Devices*, 2nd ed. (Elsevier Ltd., 2005) <https://onlinelibrary.wiley.com/doi/pdf/10.1002/0471654507.eme434>.
- [33] J. R. Lane, *Integrating Superconducting Qubits with Quantum Fluids and Surface Acoustic Wave Devices*, Ph.D. thesis, Michigan State University (2021).
- [34] B. R. Mollow, Power spectrum of light scattered by two-level systems, *Phys. Rev.* **188**, 1969 (1969).
- [35] M. Baur, S. Filipp, R. Bianchetti, J. M. Fink, M. Göppl, L. Steffen, P. J. Leek, A. Blais, and A. Wallraff, Measurement of Autler-Townes and Mollow transitions in a strongly driven superconducting qubit, *Phys. Rev. Lett.* **102**, 243602 (2009).
- [36] D. M. Toyli, A. W. Eddins, S. Boutin, S. Puri, D. Hover, V. Bolkhovskiy, W. D. Oliver, A. Blais, and I. Siddiqi, Resonance fluorescence from an artificial atom in squeezed vacuum, *Phys. Rev. X* **6**, 031004 (2016).
- [37] P. M. Harrington, M. Naghiloo, D. Tan, and K. W. Murch, Bath engineering of a fluorescing artificial atom with a photonic crystal, *Phys. Rev. A* **99**, 052126 (2019).
- [38] G. Lindblad, On the generators of quantum dynamical semigroups, *Communications in Mathematical Physics* **48**, 119 (1976).
- [39] Y. Liu and A. A. Houck, Quantum electrodynamics near a photonic bandgap, *Nature Physics* **13**, 48 (2017).
- [40] A. A. Clerk, M. H. Devoret, S. M. Girvin, F. Marquardt, and R. J. Schoelkopf, Introduction to quantum noise, measurement, and amplification, *Rev. Mod. Phys.* **82**, 1155 (2010).

- [41] M. Naghiloo, M. Abbasi, Y. N. Joglekar, and K. W. Murch, Quantum state tomography across the exceptional point in a single dissipative qubit, *Nature Physics* **15**, 1232 (2019).
- [42] J. Koch, T. M. Yu, J. Gambetta, A. A. Houck, D. I. Schuster, J. Majer, A. Blais, M. H. Devoret, S. M. Girvin, and R. J. Schoelkopf, Charge-insensitive qubit design derived from the Cooper pair box, *Phys. Rev. A* **76**, 042319 (2007).

ACKNOWLEDGEMENTS

We thank M.I. Dykman, A. Schleusner, D. Kowsari, and L. Zhang for valuable discussions. We also thank R. Loloee and B. Bi for technical assistance and use of the W. M. Keck Microfabrication Facility at MSU. The Michigan State portion of this work was supported by the National Science Foundation (NSF) via grant number ECCS-2142846 (CAREER) and the Cowen Family Endowment at MSU. C.A.M acknowledges support from the NSF via grant number DMR-1708331. The Washington University portion of this work was also supported by the NSF via grant number PHY-1752844 (CAREER).

METHODS

Qubit Fabrication

The qubit was fabricated on high resistivity silicon of thickness $275 \mu\text{m}$ using the Dolan bridge technique using a bilayer of MMA/EL9 and PMMA/C2 resists. Two Josephson junctions fabricated in parallel formed a SQUID loop with an area $16 \mu\text{m}^2$. Base exposure doses for the formation of the Josephson junctions were $300 \mu\text{C}/\text{cm}^2$ with an additional dose of $50 \mu\text{C}/\text{cm}^2$ in order to form an undercut to ensure good lift off. Superconducting wire was wound 30 times around the copper cavity into which the qubit was mounted, corresponding to one flux quantum threading the SQUID loop at $I_{\text{wire}} \sim 125 \text{ mA}$.

SAW Fabrication

The SAW resonator was fabricated on single crystal YZ-cut lithium niobate of thickness $500 \mu\text{m}$. We use a single layer PMMA/C2 resist spun at 4000 RPM for 45 sec which is then baked at 180°C and covered with a 30 nm aluminum discharging layer prior to electron beam lithography. Regions on the substrate with low spatial density of features are exposed with a dose of $325 \mu\text{C}/\text{cm}^2$, while areas with higher density of features are exposed with a

lower dose of $275 \mu\text{C}/\text{cm}^2$ to account for a lower proximity dose due to forward scattering of incident electrons. After exposure, the aluminum discharging layer is removed by submerging the sample in AZ 300 MIF developer for 200 sec. The exposed resist is then developed in a solution of 1:3 MIBK-IPA solution for 50 sec followed by 15 sec in IPA. After development, a 30 nm aluminum layer is thermally evaporated onto the substrate to form the SAW resonator structure followed by a lift-off procedure.

Hybrid System Assembly

Spacers patterned on the SAW chip of $4 \mu\text{m}$ thick S1813 photoresist nominally dictate the spacing between the qubit chip and the SAW chip. These spacers are formed by spinning four individual layers of resist at 5000 RPM for 50 sec each, followed by baking the resist at 110°C following each layer. The spacers are then patterned via standard photolithographic techniques. To make the spacers robust, the resist is then hard-baked at 250°C for 1.5 hours. The $250 \times 250 \mu\text{m}$ antenna pads on both the qubit and SAW chip are then aligned using a standard mask aligner and glued together using additional S1813 resist. Based on the coupling strength of $g_m = 12 \pm 0.6 \text{ MHz}$, we calculate the coupling capacitance between the qubit and SAW resonator to be 31.7 fF [42]. This value is slightly smaller than expected, indicating that the chips are farther apart than the thickness of the resist spacers, suggesting that the resist used for glue is dominating the inter-chip spacing [33].

Supplemental Information

SAW RESONATOR DESIGN AND MODELING

The spectral response of the SAW resonator was calculated using coupling-of-modes (COM) [1]. The periodicity of the SAW interdigitated transducer (IDT) structure is fabricated to be $\lambda_{\text{IDT}} = 800$ nm. The periodicity of the mirror structure is fabricated to be slightly larger than the periodicity of the IDT structure ($\lambda_{\text{mirror}} = 816$ nm) to guarantee a single sharply peaked resonant acoustic mode within the stopband of the mirrors where phonons are strongly reflected, which produces the confined acoustic resonance at 4.46 GHz. A list of the complete SAW device parameters are listed in Table S1. We calculate the relevant scattering parameters for each structure in the SAW resonator using coupling-of-modes with the results shown below in Fig. S1.

Parameter	Physical quantity	Value
λ_{IDT}	Transducer periodicity	800 nm
λ_{mirror}	Mirror periodicity	816 nm
N_P	Number of finger pairs	16
W	Finger pair overlap	35 μm
v_{sound}	Speed of sound	3638 m/s
η	SAW propagation loss	500 Np/m
r_i	Transducer reflectivity	-0.005i
r_m	Mirror reflectivity	-0.005i
L_{mirror}	Bragg mirror length	240.72 μm
L_{IDT}	Transducer length	12 μm

TABLE S1. Summary of fabrication parameters for the SAW resonator used in the experiment

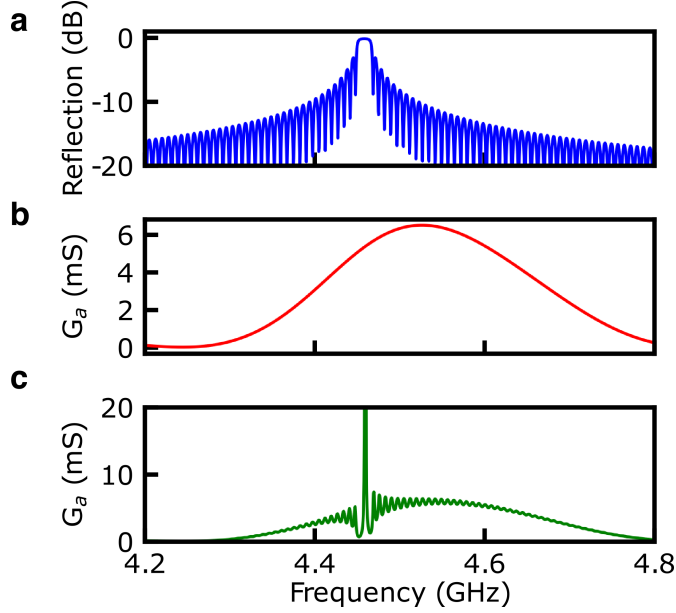


FIG. S1. (a) Simulated reflection of the Bragg mirror structure in the SAW resonator. (b) Simulated conductance of the SAW transducer, which is centered between the two acoustic Bragg mirrors. (c) Composite conductance of the SAW transducer cascaded with the mirror structure, leading to a single confined SAW mode near 4.46 GHz and a continuous conductance associated with the leakage of SAW energy through the Bragg mirrors.

NUMERICAL CALCULATION OF LINDBLAD DYNAMICS

Given a periodic drive coupling to the σ_x operator with Rabi frequency Ω , the Hamiltonian that describes the qubit in the frame rotating at ω_d is given by

$$H = \frac{\Delta}{2}\sigma_z + \frac{\Omega}{2}\sigma_x, \quad (\text{S.1})$$

where $\Delta = \omega_d - \omega_q$ is the qubit-drive detuning. In the presence of the drive, the corresponding qubit eigenstates ($|g\rangle, |e\rangle$) are rotated to a dressed basis ($|\tilde{g}\rangle, |\tilde{e}\rangle$), corresponding to the eigenvectors of Eq. S.1:

$$\begin{aligned} |\tilde{g}\rangle &= \cos\theta |g\rangle - \sin\theta |e\rangle \\ |\tilde{e}\rangle &= \sin\theta |g\rangle + \cos\theta |e\rangle, \end{aligned} \quad (\text{S.2})$$

where the rotation angle of the eigenstates is defined by $\tan 2\theta = -\Omega/\Delta$. This allows the Hamiltonian to be rewritten in the dressed basis as

$$H = \frac{\Omega_R}{2}\tilde{\sigma}_z, \quad (\text{S.3})$$

where $\Omega_R = \sqrt{\Omega^2 + \Delta^2}$ is the generalized Rabi frequency and $\tilde{\sigma}_z = \sin 2\theta\sigma_x - \cos 2\theta\sigma_z$. The evolution of the reduced density matrix in the dressed basis as given by the Lindblad master equation [2]

$$\begin{aligned} \dot{\rho} = & i[\rho, H] + \gamma_0 \cos^2(\theta) \sin^2(\theta) \mathcal{D}[\tilde{\sigma}_z]\rho + \gamma_- \sin^4(\theta) \mathcal{D}[\tilde{\sigma}_+]\rho + \\ & \gamma_+ \cos^4(\theta) \mathcal{D}[\tilde{\sigma}_-]\rho + \gamma_1 \mathcal{D}[\sigma_-]\rho + \gamma_\phi \mathcal{D}[\sigma_z]\rho. \end{aligned} \quad (\text{S.4})$$

In Eq. S.6 ρ is the reduced density matrix, which describes the driven two level system, and $\mathcal{D}[A]\rho = (2A\rho A^\dagger - A^\dagger A\rho - \rho A^\dagger A)/2$. The rates γ_+ and γ_- are the transition rates between qubit eigenstates in the dressed basis, which sample the qubit loss at the frequencies $\omega_d \pm \Omega_R$, and γ_0 is the dephasing rate in this basis. Qubit dynamics are also impacted by global depolarization and dephasing rates γ_1 and γ_ϕ , respectively. We represent the density matrix as a vector $\rho = (\rho_{gg}, \rho_{ge}, \rho_{eg}, \rho_{ee})^T$, which is evolved in time as $\rho(t) = e^{\mathcal{L}t}\rho(0)$. The matrix \mathcal{L} represents the Lindblad operator as a 4×4 matrix that is exponentiated via the transformation $V e^{Dt} V^{-1}$, where V is the matrix that diagonalizes \mathcal{L} and D is a diagonal matrix containing the eigenvalues of \mathcal{L} . We calculate expectation values in the dressed basis by taking the trace $\langle \sigma_x \rangle = \text{Tr}(\sigma_x \rho)$ and similarly for the other components of the qubit expectation value.

-
- [1] J. R. Lane, *Integrating Superconducting Qubits with Quantum Fluids and Surface Acoustic Wave Devices*, Ph.D. thesis, Michigan State University (2021).
- [2] G. Lindblad, On the generators of quantum dynamical semigroups, *Communications in Mathematical Physics* **48**, 119 (1976).